

# Direction-Controlled Bifunctional Metasurface Polarizers

Yang Chen, Jie Gao,\* and Xiaodong Yang\*

Metasurfaces composed of in-plane subwavelength nanostructures have unprecedented capability in manipulating the amplitude, phase, and polarization states of light. Here, a unique type of direction-controlled bifunctional metasurface polarizer is proposed and experimentally demonstrated based on plasmonic stepped slit-groove dimers. In the forward direction, a chiral linear polarizer is enabled which only allows the transmission of a certain incident handedness and converts it into the specified linear polarization. In the backward direction, the metasurface functions as an anisotropic circular polarizer to selectively convert a certain linear polarization component into the desired circularly polarized transmission. The observed direction-controlled polarization selection and conversion are explained by the spin-dependent mode coupling process inside the bilayer structure. Anisotropic chiral imaging based on the proposed metasurface polarizer is further demonstrated. The results provide new degrees of freedom to realize future multifunctional photonic integrated devices for structured light conversion, vector beam generation, optical imaging and sensing, and optical communication.

## 1. Introduction


Controlling the polarization states of light is one central focus in modern photonics research. In conventional optical elements, polarization variations are accumulated during the wave propagation through refraction, absorption, and reflection.<sup>[1]</sup> However, the bulky conventional polarizers are unsuitable for the increasing requirements of device integration and miniaturization in many integrated photonics applications. Their functionalities are also highly restricted. To overcome the problems, metamaterials and metasurfaces have been developed to provide a compact solution for polarization manipulation.<sup>[2–9]</sup> Benefitting from the strong interaction between the metallic or dielectric meta-atoms and the incident wave, abrupt polarization changes are generated to enable a variety of ultrathin polarizers.<sup>[10–16]</sup> However, most of the metamaterials/metasurfaces-based polarizers can only realize one certain type of polarization manipulation. Recently, the concepts of reconfigurable and programmable metasurfaces have been introduced to enable multiple electromagnetic functionalities.<sup>[17–21]</sup> However, the fabrication and operation

of such kind of active metasurfaces is quite difficult and complicated with their applications limited to the long-wavelength region. Multilayer-structured metasurfaces are also proposed to achieve multiple functionalities,<sup>[22–26]</sup> but their fabrication is a challenging issue, especially for the requirement of accurate alignment between different layers. Besides, the metasurfaces working in off-axis reflection mode can also enable multifunctional optical devices,<sup>[27–29]</sup> but the off-axis design can cause much inconvenience and beam misalignment during the optical setup building and output beam capturing process, and it is also incompatible with commonly used on-axis optical setups. Moreover, metasurfaces composed of anisotropic nanostructures can perform different optical modulations in the two orthogonal directions,<sup>[30,31]</sup> but the plasmonic cross-talk between the two directions can worsen their optical performance.

Asymmetric transmission, as an important manifestation of optical chirality, provides an alternative avenue to realize bifunctional polarizers. Owing to the direction-dependent polarization conversion of the incident handedness into the opposite handedness, different total transmission is generated when light with certain polarization impinges from opposite sides of the chiral media.<sup>[22,32–34]</sup> Although the time reversal of light interaction with chiral structures is broken, the reciprocity lemma is still preserved. In the past decades, chiral metamaterials and metasurfaces with distinguished optical responses to left-handed and right-handed circularly polarized (LCP and RCP) light have been extensively developed to enable various types of polarizers.<sup>[10,11,13,35–39]</sup> However, chiral metamaterials or metasurfaces with specifically tailored asymmetric transmission for performing distinct polarization manipulation on oppositely incident light have not been reported yet. For three-dimensional (3D) chiral metamaterials, their fabrication methods are either complicated and time-consuming, like the stacking lithography method<sup>[11,38,40]</sup> and electron/ion beam-induced deposition method,<sup>[41,42]</sup> or lack of flexibility and reproducibility, like the DNA-assisted self-assembly method<sup>[43]</sup> and glancing-angle deposition technique.<sup>[44,45]</sup> But for two-dimensional chiral metasurfaces with much lower fabrication difficulties, they are not truly chiral and hence suffer from weak chiroptical response.<sup>[36,46,47]</sup>

In this work, we propose and experimentally demonstrate a new type of chiral metasurfaces based on plasmonic stepped slit-groove dimers to realize direction-controlled bifunctional

Dr. Y. Chen, Prof. J. Gao, Prof. X. Yang  
Department of Mechanical and Aerospace Engineering  
Missouri University of Science and Technology  
Rolla, MO 65409, USA  
E-mail: gaojie@mst.edu; yangxia@mst.edu

 The ORCID identification number(s) for the author(s) of this article can be found under <https://doi.org/10.1002/lpor.201800198>

DOI: 10.1002/lpor.201800198

metasurface polarizers. The stepped metasurface with truly chiral geometries can be easily fabricated using one-step grayscale focused ion beam milling method. In the forward direction, the metasurface acts as a chiral linear polarizer only allowing the transmission of a certain incident handedness, which is converted to linearly polarized (LP) output light orientated almost orthogonally to the slit. The circular dichroism in transmission (CDT) as large as 0.85 is experimentally achieved. In the backward direction, the metasurface functions as an anisotropic circular polarizer, which selectively converts the linear polarization component along the normal direction of the slit into the desired circularly polarized transmission. These unprecedented optical properties are attributed to the circularly dichroic mode coupling process between the two layers of the stepped slit-groove dimer structure. Anisotropic chiral imaging based on the proposed metasurface polarizer is further presented as one promising application with unique functionalities. Our work provides a versatile platform for multiplexed optical elements,<sup>[48,49]</sup> complex vector beam generation,<sup>[50,51]</sup> optical imaging and sensing, and optical information processing.<sup>[52,53]</sup>

## 2. Experimental Section

### 2.1. Metasurface Fabrication

The plasmonic metasurface was milled in a 180 nm-thick gold film on a silica substrate using focused ion beam system (FEI Helios Nanolab 600, 30 kV, 9.7 pA). The focus and astigmatism of the ion beam was finely optimized. The different depths of slits and grooves were realized by applying different ion doses, which were defined by pre-edited grayscale *bmp* patterns. The redeposition effect was considered and compensated during the grayscale pattern design (see Section S1, Supporting Information). To capture the cross-sectional SEM images, a layer of platinum was first deposited onto the sample using electron-beam-induced deposition. Then, a trench was etched through into the substrate to expose the cross section of the stepped slit-groove dimer structure.

### 2.2. Numerical Simulations

All simulations were conducted using a commercially available finite element solver COMSOL Multiphysics. The permittivity of gold was obtained from spectroscopic ellipsometry data fitted with a general oscillator model, and the refractive index of silica was set as 1.45. The simulation unit was enclosed by periodic boundary conditions in the *x*- and *y*-directions, and it was truncated by perfectly matched layers surrounded by scattering boundaries in the *z*-direction. All the sharp corners of the structure were rounded with a radius of curvature of 10 nm to avoid possible numerical artifacts.

### 2.3. Experimental Setup

To analyze the output polarization from the metasurface, a collimated broadband Tungsten–Halogen light source was illumina-

ted vertically onto the metasurface sample, and the transmitted light was directed through a rotating linear polarizer and then received by an optical spectrometer (Horiba, iHR550). In order to perform the anisotropic chiral imaging, a collimated laser beam with tunable wavelength was emitted from a Ti:Sapphire oscillator (Spectra-Physics Tsunami), directed through a linear polarizer cascaded with a quarter-wave plate, and then focused loosely onto the metasurface sample by a lens. The transmitted light was collected by a 20× objective through a linear polarizer and then captured by an infrared-CCD camera.

## 3. Results and Discussion

### 3.1. Chiral Metasurface Design

The chiral metasurface is composed of an array of plasmonic stepped slit-groove dimers etched in an optically thick gold film, where the consisting slit and groove having the same rectangular shape are arranged with a flare angle  $\theta$  and a spacing gap  $g$  in each unit cell (**Figure 1a**). Geometric parameters of the metasurface are optimized as described in Section S2, Supporting Information. Depending on whether the slit is on the left or on the right, the slit-groove dimer lacking any mirror symmetry exists in two enantiomeric forms of Form A and Form B. Distinguished from the unit-cell structures of conventional metasurfaces where nanoantennas or nanoapertures possess the uniform thickness or depth, the stepped slit-groove dimer structure has two different depths  $H$  and  $h$ , so that symmetry breaking is introduced along the propagation direction to provide a truly chiral geometry. On the other hand, compared to conventional metamaterials with complex 3D geometries, rectangular slits and grooves, as the basic building blocks of the proposed metasurface, are easy to fabricate using one-step grayscale focused ion beam milling method. Moreover, rectangular slits and grooves are among the most fundamental structures used in plasmonics, offering the generality for our design to be extended to structures with other geometries. The fabricated chiral metasurface samples are shown in **Figure 1b**. The realistic sidewalls are tapered instead of vertical due to the fabrication process, which is discussed in Section S3, Supporting Information.

### 3.2. Metasurface Chiral Linear Polarizer in the Forward Direction

Here, the forward direction is defined as the incoming waves are illuminated onto the metal surface and transmitted out of the dielectric substrate (**Figure 2a**). The chiroptical properties of the metasurface in Form A are first examined in the forward direction by full-wave electromagnetic simulations. A prominent transmission resonance is observed at 724 nm under RCP incidence, while the transmission under LCP incidence at this wavelength is almost totally suppressed (**Figure 2b**). The corresponding circular dichroism in transmission  $CDT = (T_{RCP} - T_{LCP}) / (T_{RCP} + T_{LCP})$  is calculated to be 1.0, where the transmission under RCP incidence  $T_{RCP} = T_{RCP/RCP} + T_{RCP/LCP}$  and the transmission under LCP incidence  $T_{LCP} = T_{LCP/RCP} + T_{LCP/LCP}$ .  $T_{RCP/LCP}$  indicates the LCP

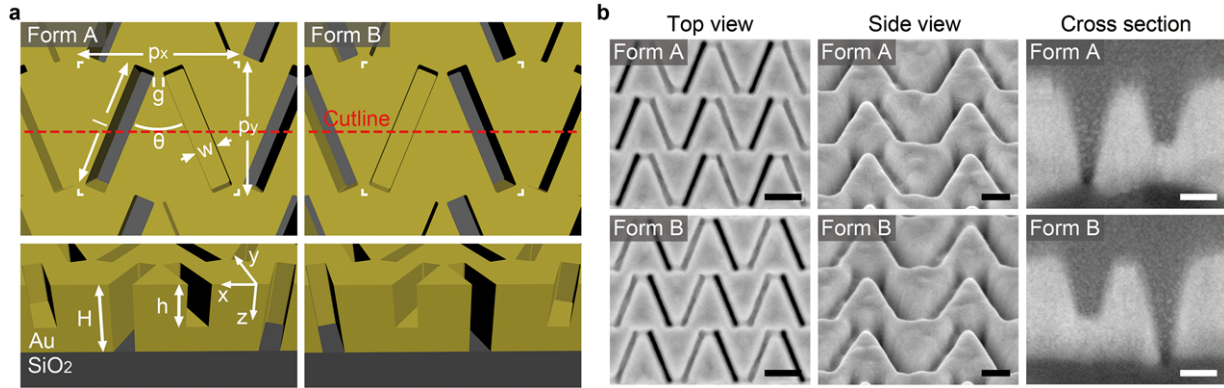


**Figure 1.** Chiral unit cell design. a) Schematic of the chiral stepped slit-groove dimer in its two enantiomeric forms (Form A and Form B). Their cross-sectional views are illustrated at the bottom corresponding to the red dashed cutlines in the top panels. The geometric parameters are indicated as  $p_x = 360$  nm,  $p_y = 300$  nm,  $g = 20$  nm,  $l = 300$  nm,  $w = 50$  nm,  $\theta = 45^\circ$ ,  $H = 180$  nm,  $h = 110$  nm. b) SEM images of the fabricated chiral metasurfaces in Form A and Form B. Side view images and cross-sectional images are captured with a visual angle of  $52^\circ$  to the surface normal. The scale bars are 200, 100, and 50 nm from left to right.

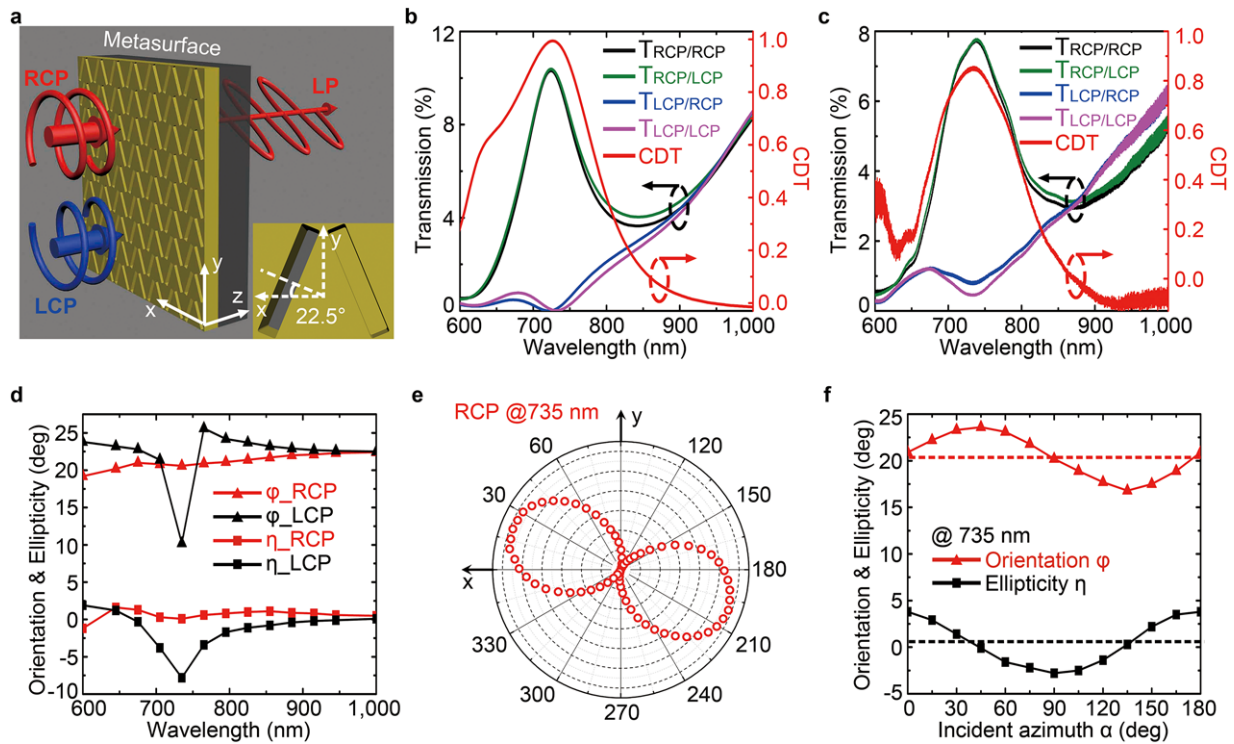


**Figure 2.** Chiral linear polarizer in the forward direction. a) Schematic illustration of the metasurface used as chiral linear polarizer when circularly polarized light is incident in the forward ( $+z$ )-direction. One unit-cell structure is shown in the inset with the indicated normal direction of the slit. Transmission spectra of the metasurface in Form A for different incident/output handedness combinations together with the corresponding CDT spectra obtained from b) simulations and c) experiments in the forward direction. d) Measured spectral dependence of the output polarization orientation angle  $\varphi$  and ellipticity angle  $\eta$  for the metasurface in Form A under RCP and LCP incidence. e) Polar diagram of the output polarization measured under RCP incidence at 735 nm. f)  $\varphi$  and  $\eta$  measured as a function of the azimuthal angle  $\alpha$  of the LP incident light at 735 nm. The dashed lines indicate their average values.

transmission under RCP incidence and the other three components ( $T_{RCP/RCP}$ ,  $T_{LCP/RCP}$ ,  $T_{LCP/LCP}$ ) are defined in the same way. In accordance with the simulations, experimental results exhibit a CDT resonance of 0.85 at 735 nm (Figure 2c), which is significantly larger than most of the existing chiral metamaterials and metasurfaces.<sup>[36,37,41,54–58]</sup> The discrepancies between the simula-

tion and experimental results could come from the fabrication tolerance of the focused ion beam milling method, the roughness of the gold film, and the imperfections of the linear polarizer and quarter-wave plate in the experimental setup. Among the transmitted light under RCP incidence, the RCP and LCP components coincide with each other (Figure 2b,c), leading to good

polarization linearity with the ellipticity angle  $\eta$  below  $2.0^\circ$  ranging from 600 to 1000 nm (Figure 2d). The output polarization orientation angle  $\varphi$  is measured to be nearly orthogonal to the slit. For LCP incidence, the output polarization is also approximately linearly polarized along the normal direction of the slit, except for the wavelength range around the CDT resonance of 735 nm where the transmitted RCP component is considerably stronger than the LCP component, resulting in elliptical polarization with large  $\eta$ . Polar diagram of the output polarization under RCP incidence at 735 nm is illustrated in Figure 2e, showing a typical linear polarization pattern. Accordingly, a spin-selective chiral linear polarizer is enabled in the forward direction to only allow the transmission of RCP incidence and convert it into linear polarization with the orientation angle approximately normal to the slit.

Moreover, the output polarization state of the metasurface under LP incidence is investigated. In order to eliminate the influence of linear birefringence caused by the residual anisotropy of the unit-cell structure, polarization analysis is performed for incident azimuthal angles  $\alpha$  over a  $180^\circ$  period to obtain average values of  $\varphi$  and  $\eta$  at 735 nm, which match well with the RCP incidence case (Figure 2f). Linearly polarized transmission is generated under LP incidence, indicating that the metasurface acts as a chiral linear polarizer rather than a chiral quarter waveplate in the forward direction. It is noted that the absolute orientation angle  $\varphi$ , rather than the rotation angle  $\psi = \varphi - \alpha$ , is oscillating periodically with the incident azimuth  $\alpha$ , indicating the disappearance of optical rotation (OR) for the current chiral metasurface.

### 3.3. Chiroptical Analysis for the Stepped Slit-Groove Dimer

For most of the chiral metamaterials and metasurfaces, optical rotation and circular dichroism (CD) are linked by the Kramers–Kronig relations, because they are originated respectively from the real and imaginary part of the refractive index.<sup>[40,59,60]</sup> The circularly dichroic imaginary part generally stems from spin-dependent near-field distributions inside chiral structures and the corresponding ohmic loss in metal,<sup>[32,33]</sup> as well as substrate effects.<sup>[36,61]</sup> As a result, a LP wave is azimuthally rotated for the existence of OR, while its polarization state is converted to elliptical polarization or circular polarization by CD. Generally, only when CD is eliminated can LP transmission be generated.<sup>[54,56]</sup> Nevertheless, our proposed metasurface provides a new avenue to enable linearly polarized transmission without optical rotation over a broad spectrum, even though high CDT is presented as well, because the high CDT is originated from the circularly dichroic mode coupling process inside the stepped structure.

We start with the basic rectangular groove structure. Only when the incident polarization is orthogonal to the groove can surface plasmons be efficiently excited and coupled into the groove to induce the fundamental  $TE_{10}$  mode<sup>[62]</sup> (Figure 3a). Electric dipole features are manifested, as well as two antiparallel magnetic dipoles surrounded by two surface currents in opposite directions (Figure 3b). Next, we consider the groove dimer structure as shown in the inset of Figure 3c. When an  $x$ -polarized wave is illuminated, the upper circulating currents of the two grooves have the same direction as well as the resulting magnetic

dipoles (Figure 3d), introducing a repulsive interaction between the two grooves via the surface current and magnetic field.<sup>[63–65]</sup> Therefore, the symmetric plasmonic mode of the groove dimer structure is blueshifted relative to the  $TE_{10}$  mode of a single groove (Figure 3c). Similarly, an attractive interaction is formed between the two grooves under  $y$ -polarized incidence, leading to the antisymmetric plasmonic mode redshifted for the groove dimer structure. Meanwhile, the induced electric dipoles of the two grooves oscillate in phase with each other for the symmetric mode, and out of phase for the antisymmetric mode (Figure 3e). When circularly polarized excitation is applied, the two plasmonic modes are simultaneously excited with a relative phase delay of  $90^\circ$  or  $-90^\circ$  and interfere with each other to generate the orthogonal RCP and LCP modes (Figure 3e). For the RCP mode, the interference is constructive at the left arm and destructive at the right arm, resulting in electric field highly enhanced at the left arm and extremely weak at the right arm, which is reversed for the LCP mode. Such near-field chirality is resonant at 724 nm, where the symmetric and antisymmetric modes possess the largest spectral overlap, even though no chirality is observable in the far field.

Furthermore, the stepped slit-groove dimer design can be regarded as a bilayer structure, where the groove dimer structure at the top layer is connected with a rectangular slit at the bottom layer on the left or right for Form A or B. When RCP wave at 724 nm is illuminated on the metasurface in Form A, electric field is highly enhanced at the left arm of the top-layer groove dimer structure, exhibiting electric dipole features (Figure 3f). This part of field is then coupled to the  $TE_{10}$  mode of the bottom-layer slit to form the large transmission, with the polarization orthogonal to the slit owing to the dipole emission of the  $TE_{10}$  mode (Figure 3f). But for the LCP case, the transmission is extremely low at this wavelength due to the selective concentration of local field to the right arm at the top layer. Higher-order modes, together with the  $TE_{10}$  mode, are then induced in the bottom-layer slit to generate the elliptically polarized transmission (Figure 3f). It is noted that the CDT resonance of the stepped metasurface matches perfectly with the near-field chirality resonance of the groove dimer structure. Optical power flow distributions in Figure 3g further reveal that the incoming RCP wave is sorted into the left slit and transmitted through the metal film, while the incident LCP wave is selectively focused into the right groove and then reflected back. In fact, our proposed chiral metasurface offers a new design scheme with the chirality relying on the spin-dependent mode coupling process between the top layer and the bottom layer instead of the circularly dichroic absorption. The consisting slit and groove structures can be designed in other shapes such as L-shape and arc-shape, which are demonstrated in Section S4, Supporting Information.

### 3.4. Metasurface Anisotropic Circular Polarizer in the Backward Direction

The optical properties of the metasurface in the backward direction are then characterized (Figure 4a). Circular Jones transmission matrix of the metasurface in the forward direction at 724 nm can be retrieved from simulations as



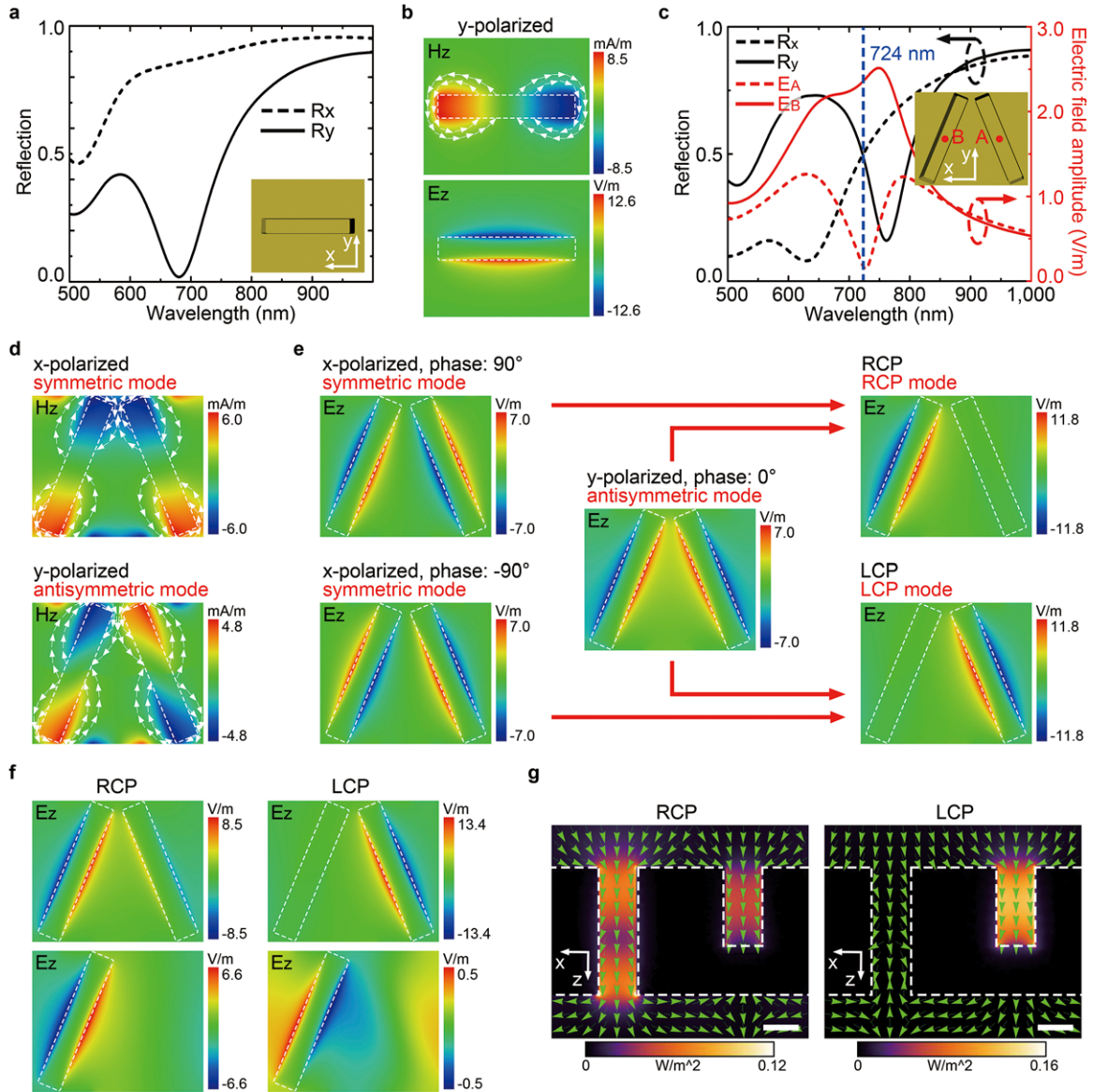


**Figure 3.** Chiroptical analysis for the stepped slit-groove dimer in the forward direction. a) Simulated reflection spectra of an array of rectangular grooves under x-polarized and y-polarized incidence. The unit-cell period and groove geometry shown in the inset are the same with those in Figure 1a. b) Longitudinal magnetic and electric field distributions  $H_z$  and  $E_z$  plotted 4 nm above the groove under y-polarized incidence at 680 nm. The white arrows illustrate the flow of induced surface currents. c) Simulated reflection spectra of an array of rectangular groove dimers under x-polarized and y-polarized illumination, together with the electric field amplitude extracted respectively from the two grooves ( $E_A$  and  $E_B$ ) under RCP incidence. The field points A and B are 4 nm above the bottom of the two grooves. The groove dimer structure as depicted in the inset is constructed by replacing the slit with an identical groove. d)  $H_z$  distributions of the groove dimer structure under x-polarized and y-polarized illumination at 724 nm, together with the induced surface current distributions indicated by the white arrows. e)  $E_z$  distributions of the groove dimer structure under x-polarized and y-polarized incidence at 724 nm with certain phase delay, and the resulting  $E_z$  distributions under RCP and LCP illumination. f)  $E_z$  distributions of the stepped slit-groove dimer structure in Form A under RCP and LCP incidence at 724 nm, which are plotted 4 nm above the top surface (top row) and 4 nm below the bottom surface (bottom row). g) Optical power flow distributions of the slit-groove dimer structure in Form A under RCP and LCP illumination at 724 nm. The background colors and field arrows indicate the magnitude and direction of the Poynting vectors. Scale bar: 50 nm.

$$T_{\text{circ}}^{\text{F}} = \begin{bmatrix} T_{\text{RCP/RCP}}^{\text{F}} & T_{\text{LCP/RCP}}^{\text{F}} \\ T_{\text{RCP/LCP}}^{\text{F}} & T_{\text{LCP/LCP}}^{\text{F}} \end{bmatrix} = \begin{bmatrix} 0.35e^{1.39i} & 0.017e^{0.94i} \\ 0.35e^{-2.36i} & 0.022e^{0.85i} \end{bmatrix} \quad (1)$$

where  $T_{\text{LCP/RCP}}^{\text{F}}$  indicates the RCP transmission under LCP incidence in the forward direction. According to the Lorentz reciprocity theorem, the Jones transmission matrix in the backward direction can be expressed as<sup>[66]</sup>

$$T_{\text{circ}}^{\text{B}} = \begin{bmatrix} T_{\text{RCP/RCP}}^{\text{B}} & T_{\text{LCP/RCP}}^{\text{B}} \\ T_{\text{RCP/LCP}}^{\text{B}} & T_{\text{LCP/LCP}}^{\text{B}} \end{bmatrix} = \begin{bmatrix} T_{\text{RCP/RCP}}^{\text{F}} & -T_{\text{RCP/LCP}}^{\text{F}} \\ -T_{\text{LCP/RCP}}^{\text{F}} & T_{\text{LCP/LCP}}^{\text{F}} \end{bmatrix} \\ = \begin{bmatrix} 0.35e^{1.39i} & 0.35e^{2.36i} \\ 0.017e^{-0.94i} & 0.022e^{0.85i} \end{bmatrix} \quad (2)$$

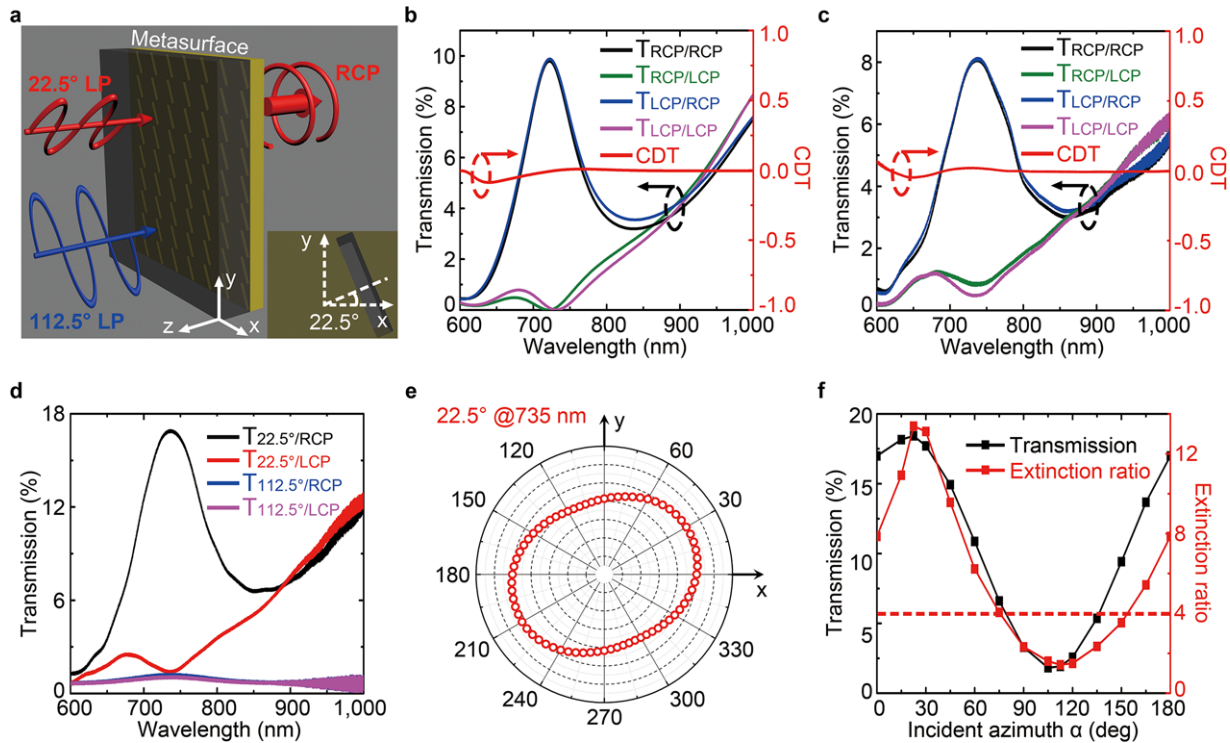


**Figure 4.** Anisotropic circular polarizer in the backward direction. a) Illustration of the metasurface acting as anisotropic circular polarizer when LP light is illuminated in the backward ( $-z$ )-direction. One unit-cell structure is depicted in the inset with the indicated normal direction of the slit. Transmission spectra of the metasurface in Form A for different incident/output handedness combinations together with the corresponding CDT spectra acquired from b) simulations and c) experiments in the backward direction. d) Measured transmission spectra of the RCP and LCP components for LP incidence of  $22.5^\circ$  and  $112.5^\circ$ .  $T_{22.5^\circ/\text{RCP}}$  represents the RCP transmission under LP incident of  $22.5^\circ$ . e) Polar diagram of the output polarization measured under LP incidence of  $22.5^\circ$  at 735 nm. f) Total transmission and extinction ratio measured as a function of the azimuthal angle  $\alpha$  of the LP incident light at 735 nm.

where  $T_{\text{LCP/RCP}}^{\text{B}}$  represents the RCP transmission under LCP incidence in the backward direction. It is suggested that both RCP and LCP incoming waves are transmitted to possess the RCP spin in the backward direction, which is further confirmed by the simulated and measured transmission spectra (Figure 4b,c). Compared to the forward transmission spectra shown in Figure 2b,c, only the two cross-polarized components  $T_{\text{RCP/LCP}}$  and  $T_{\text{LCP/RCP}}$  are exchanged for the backward transmission spectra, resulting in almost zero CDT over a broad spectrum. Although no spin selectivity is exhibited for the metasurface in the backward direction, high linear anisotropy is presented instead, where LP light along the normal or parallel direction of the slit is preferentially transmitted or blocked (Figure 4d). Among the transmitted light for the LP incidence of  $22.5^\circ$ , the extinction ratio between the RCP component and LCP component can be as large as 13.4 at 735 nm. The corresponding polar diagram shows a typical circular polarization pattern (Figure 4e), although it is not perfect. Furthermore, total transmission and extinction ratio are evaluated over a  $180^\circ$  period of the incident azimuthal angle  $\alpha$  (Figure 4f), where the total transmission approximately follows the relationship  $T = \cos^2(\alpha - 22.5^\circ)$ . A high extinction ratio of over 4 is maintained across the broad  $\alpha$  range from  $0^\circ$  to  $75^\circ$  and from  $155^\circ$  to  $180^\circ$ . When the  $\alpha$  value is around  $112.5^\circ$ , the extinction ratio is low and the total transmission is also substantially suppressed. Since circularly polarized transmission is generated under both

linearly polarized and circularly polarized incidence, the metasurface functions as an anisotropic circular polarizer in the backward direction to only accept the incident linear polarization component along a certain direction and then convert it to circular polarization.

The optical properties of the metasurface in the backward direction can also be attributed to the circularly dichroic mode coupling process inside the structure. At the entrance plane of the metasurface, rectangular slits are facing the incoming waves. Thus, no spin selectivity is exhibited, and only the incident linear polarization component orthogonal to the slit is coupled into the top-layer slit to induce the  $TE_{10}$  mode, which shares better field overlap with the RCP mode of the bottom-layer groove dimer structure. Consequently, rather than LCP mode, RCP mode is excited inside the bottom layer to generate the strong RCP transmission.

### 3.5. Anisotropic Chiral Imaging

As an important application for chiral metamaterials and metasurfaces, chiral imaging has been studied to achieve different displayed images by switching the incident handedness.<sup>[39,67]</sup> Here, a new degree of freedom in polarization-controllable

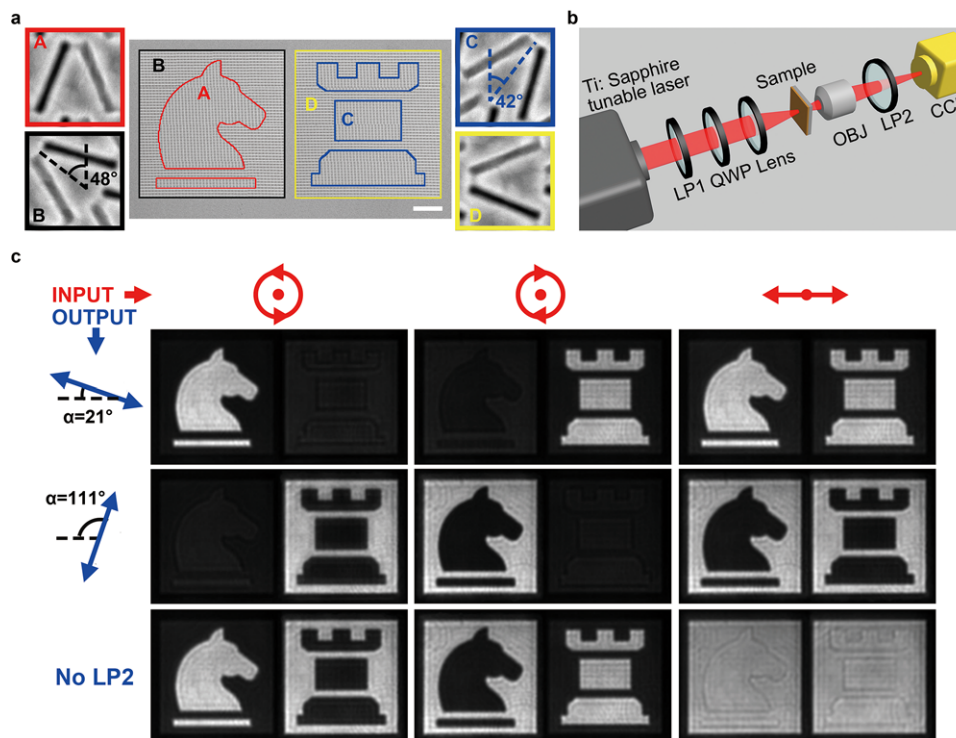


**Figure 5.** Anisotropic chiral imaging enabled by the metasurface polarizer in the forward direction. a) SEM images of the chess pattern divided into four areas, which are composed of four kinds of unit cells, respectively. The cells A and D in Form A are orientated vertically and horizontally, while the cells B and C in Form B are orientated at certain angles. Scale bar: 10  $\mu\text{m}$ . b) Schematic experimental setup for anisotropic chiral imaging. LP, linear polarizer; QWP, quarter-wave plate; OBJ, objective. c) Transmission images of the chess pattern captured at 735 nm under RCP (Column 1), LCP (Column 2), and LP (Column 3) illumination. The output polarization is also chosen by rotating (Rows 1 and 2) or removing (Row 3) the LP2.

imaging is realized by the combination of input handedness and output linear polarization in the forward direction, or the combination of input linear polarization and output handedness in the backward direction. According to the Lorentz reciprocity theorem, here only the anisotropic chiral imaging experiments in the forward direction are conducted. A chess pattern is designed and fabricated, where four areas are composed of four different unit cells (Figure 5a). Cell A and cell C with opposite spin selectivity share the same output linear polarization direction, which is vertical to that of cell B and cell D. The experimental setup for image modulation and acquisition is illustrated in Figure 5b. By varying the combinations of input and output polarizations, nine different images are displayed (Figure 5c). It is observed from any single row that chiral image contrast (CIC) is large by switching the input handedness for the metasurface in the forward direction, while anisotropic image contrast (AIC) is also manifested to be high from any single column by selecting the output linear polarization. Without loss of generality, the CIC and AIC can be calculated based on the top-left image.  $\text{CIC} = (I_A - I_C) / (I_A + I_C)$  is calculated to be 81%, and  $\text{AIC} = (I_A - I_D) / (I_A + I_D)$  is 78%, where  $I_A$  ( $I_C$  or  $I_D$ ) represents the average brightness of the area A (C or D). Therefore, anisotropic chiral imaging with high image contrast is demonstrated for the first time based on the metasurface chiral linear polarizer in the forward direction. Broadband properties of the imaging are discussed in Section S5, Supporting Information.

#### 4. Conclusions and Outlook

In summary, we have developed and demonstrated a novel concept of chiral metasurfaces based on plasmonic stepped slit-groove dimers for achieving direction-controlled bifunctional metasurface polarizers. The metasurface functions as chiral linear polarizer in the forward direction, where circularly polarized light with certain spin is selectively transmitted and converted to the specified linearly polarized light with ultrahigh CDT value. Meanwhile, the metasurface behaves as anisotropic circular polarizer in the backward direction, which only accepts certain linear polarization component and converts it into the desired circular polarization. The unique optical properties stem from the circularly dichroic mode coupling process inside the bilayer stepped slit-groove dimer structure, opening a new avenue for designing easy-to-fabricate chiral metasurfaces with strong chiroptical responses. Moreover, anisotropic chiral imaging is demonstrated based on the metasurface as a manifestation of its intriguing functionality. It is noted that the absolute working efficiency of the bifunctional polarizer device is measured to be 15.5% and 17.0% in the forward and backward directions at 735 nm, which is not high owing to the large Ohmic loss of the gold film. To further boost the efficiency, it is promising to adopt dielectric films with lower absorption, such as  $\text{TiO}_2$  and Si, to replace the gold film in the future work.<sup>[48,49]</sup> The proposed bifunctional metasurface polarizers will highly extend the



capabilities of the existing metamaterials and metasurfaces for advancing a variety of applications in polarization manipulation, complex vector beam generation, imaging and sensing, optical information processing, and optical communication.

## Supporting Information

Supporting Information is available from the Wiley Online Library or from the author.

## Acknowledgements

The authors acknowledge support from the Office of Naval Research under Grant No. N00014-16-1-2408, and the National Science Foundation under Grant No. ECCS-1653032 and DMR-1552871. The authors thank the facility support from the Materials Research Center at Missouri S&T.

## Conflict of Interest

The authors declare no conflict of interest.

## Keywords

3D fabrication, asymmetric transmission, chiral metasurfaces, circular dichroism, polarization conversion

Received: July 26, 2018  
Revised: September 1, 2018  
Published online:

- [1] M. Born, E. Wolf, A. B. Bhatia, *Principles of Optics: Electromagnetic Theory of Propagation, Interference and Diffraction of Light*, Vol. 7, Cambridge University Press, Cambridge 1999.
- [2] S. Sun, Q. He, S. Xiao, Q. Xu, X. Li, L. Zhou, *Nat. Mater.* **2012**, *11*, 426.
- [3] N. Shitrit, I. Yulevich, E. Maguid, D. Ozeri, D. Veksler, V. Kleiner, E. Hasman, *Science* **2013**, *340*, 724.
- [4] X. Yin, Z. Ye, J. Rho, Y. Wang, X. Zhang, *Science* **2013**, *339*, 1405.
- [5] N. K. Grady, J. E. Heyes, D. R. Chowdhury, Y. Zeng, M. T. Reiten, A. K. Azad, A. J. Taylor, D. A. Dalvit, H. T. Chen, *Science* **2013**, *340*, 1304.
- [6] N. Yu, F. Capasso, *Nat. Mater.* **2014**, *13*, 139.
- [7] A. Arbabi, Y. Horie, M. Bagheri, A. Faraon, *Nat. Nanotechnol.* **2015**, *10*, 937.
- [8] Q. He, S. Sun, S. Xiao, L. Zhou, *Adv. Opt. Mater.* **2018**, *6*, 1800415.
- [9] Y. Chen, X. Yang, J. Gao, *Adv. Opt. Mater.* **2018**, *6*, 1800646.
- [10] J. K. Gansel, M. Thiel, M. S. Rill, M. Decker, K. Bade, V. Saile, G. von Freymann, S. Linden, M. Wegener, *Science* **2009**, *325*, 1513.
- [11] Y. Zhao, M. A. Belkin, A. Alu, *Nat. Commun.* **2012**, *3*, 870.
- [12] N. Yu, F. Aieta, P. Genevet, M. A. Kats, Z. Gaburro, F. Capasso, *Nano Lett.* **2012**, *12*, 6328.
- [13] J. K. Gansel, M. Latzel, A. Frölich, J. Kaschke, M. Thiel, M. Wegener, *Appl. Phys. Lett.* **2012**, *100*, 101109.
- [14] A. Pors, S. I. Bozhevolnyi, *Opt. Express* **2013**, *21*, 2942.
- [15] F. Ding, Z. Wang, S. He, V. M. Shalaev, A. V. Kildishev, *ACS Nano* **2015**, *9*, 4111.
- [16] Y. Chen, Y. Chen, J. Chu, X. Xu, *ACS Photonics* **2017**, *4*, 567.
- [17] T. J. Cui, M. Q. Qi, X. Wan, J. Zhao, Q. Cheng, *Light: Sci. Appl.* **2014**, *3*, e218.
- [18] Q. Wang, E. T. F. Rogers, B. Gholipour, C.-M. Wang, G. Yuan, J. Teng, N. I. Zheludev, *Nat. Photonics* **2016**, *10*, 60.
- [19] K. Chen, Y. Feng, F. Monticone, J. Zhao, B. Zhu, T. Jiang, L. Zhang, Y. Kim, X. Ding, S. Zhang, A. Alu, C. W. Qiu, *Adv. Mater.* **2017**, *29*, 1606422.
- [20] L. Li, T. Jun Cui, W. Ji, S. Liu, J. Ding, X. Wan, Y. Bo Li, M. Jiang, C. W. Qiu, S. Zhang, *Nat. Commun.* **2017**, *8*, 197.
- [21] K. Chen, Y. Feng, L. Cui, J. Zhao, T. Jiang, B. Zhu, *Sci. Rep.* **2017**, *7*, 42802.
- [22] C. Pfeiffer, C. Zhang, V. Ray, L. J. Guo, A. Grbic, *Phys. Rev. Lett.* **2014**, *113*, 023902.
- [23] L. Zhang, R. Y. Wu, G. D. Bai, H. T. Wu, Q. Ma, X. Q. Chen, T. J. Cui, *Adv. Funct. Mater.* **2018**, *28*, 1802205.
- [24] T. Cai, G. Wang, S. Tang, H. Xu, J. Duan, H. Guo, F. Guan, S. Sun, Q. He, L. Zhou, *Phys. Rev. Appl.* **2017**, *8*, 034033.
- [25] J. H. Shi, H. F. Ma, C. Y. Guan, Z. P. Wang, T. J. Cui, *Phys. Rev. B* **2014**, *89*, 165128.
- [26] W. Luo, S. Sun, H.-X. Xu, Q. He, L. Zhou, *Phys. Rev. Appl.* **2017**, *7*, 044033.
- [27] F. Yue, D. Wen, C. Zhang, B. D. Gerardot, W. Wang, S. Zhang, X. Chen, *Adv. Mater.* **2017**, *29*, 1603838.
- [28] J. Hao, Y. Yuan, L. Ran, T. Jiang, J. A. Kong, C. T. Chan, L. Zhou, *Phys. Rev. Lett.* **2007**, *99*, 063908.
- [29] L. Zhang, S. Liu, L. Li, T. J. Cui, *ACS Appl. Mater. Interfaces* **2017**, *9*, 36447.
- [30] T. Cai, S. Tang, G. Wang, H. Xu, S. Sun, Q. He, L. Zhou, *Adv. Opt. Mater.* **2017**, *5*, 1600506.
- [31] W. T. Chen, K. Y. Yang, C. M. Wang, Y. W. Huang, G. Sun, I. D. Chiang, C. Y. Liao, W. L. Hsu, H. T. Lin, S. Sun, L. Zhou, A. Q. Liu, D. P. Tsai, *Nano Lett.* **2014**, *14*, 225.
- [32] V. A. Fedotov, P. L. Mladyonov, S. L. Prosvirnin, A. V. Rogacheva, Y. Chen, N. I. Zheludev, *Phys. Rev. Lett.* **2006**, *97*, 167401.
- [33] V. Fedotov, A. Schwanecke, N. Zheludev, V. Khaidikov, S. Prosvirnin, *Nano Lett.* **2007**, *7*, 1996.
- [34] C. Menzel, C. Helgert, C. Rockstuhl, E. B. Kley, A. Tunnermann, T. Pertsch, F. Lederer, *Phys. Rev. Lett.* **2010**, *104*, 253902.
- [35] A. Papakostas, A. Potts, D. M. Bagnall, S. L. Prosvirnin, H. J. Coles, N. I. Zheludev, *Phys. Rev. Lett.* **2003**, *90*, 107404.
- [36] M. Kuwata-Gonokami, N. Saito, Y. Ino, M. Kauranen, K. Jefimovs, T. Vallius, J. Turunen, Y. Svirko, *Phys. Rev. Lett.* **2005**, *95*, 227401.
- [37] M. Hentschel, M. Schaferling, T. Weiss, N. Liu, H. Giessen, *Nano Lett.* **2012**, *12*, 2542.
- [38] H. S. Park, T. T. Kim, H. D. Kim, K. Kim, B. Min, *Nat. Commun.* **2014**, *5*, 5435.
- [39] Y. Chen, J. Gao, X. Yang, *Nano Lett.* **2018**, *18*, 520.
- [40] X. Yin, M. Schaferling, B. Metzger, H. Giessen, *Nano Lett.* **2013**, *13*, 6238.
- [41] M. Esposito, V. Tasco, F. Todisco, M. Cuscuna, A. Benedetti, M. Scuderi, G. Nicotra, A. Passaseo, *Nano Lett.* **2016**, *16*, 5823.
- [42] M. Esposito, V. Tasco, M. Cuscunà, F. Todisco, A. Benedetti, I. Tarantini, M. D. Giorgi, D. Sanvitto, A. Passaseo, *ACS Photonics* **2015**, *2*, 105.
- [43] H. E. Lee, H. Y. Ahn, J. Mun, Y. Y. Lee, M. Kim, N. H. Cho, K. Chang, W. S. Kim, J. Rho, K. T. Nam, *Nature* **2018**, *556*, 360.
- [44] B. Yeom, H. Zhang, H. Zhang, J. I. Park, K. Kim, A. O. Govorov, N. A. Kotov, *Nano Lett.* **2013**, *13*, 5277.
- [45] A. G. Mark, J. G. Gibbs, T.-C. Lee, P. Fischer, *Nat. Mater.* **2013**, *12*, 802.
- [46] V. Valev, N. Smisdrom, A. Silhanek, B. De Clercq, W. Gillijns, M. Ameloot, V. Moshchalkov, T. Verbiest, *Nano Lett.* **2009**, *9*, 3945.
- [47] M. Mutlu, A. E. Akosman, A. E. Serebryannikov, E. Ozbay, *Opt. Lett.* **2011**, *36*, 1653.



- [48] D. Lin, P. Fan, E. Hasman, M. L. Brongersma, *Science* **2014**, *345*, 298.
- [49] M. Khorasaninejad, W. T. Chen, R. C. Devlin, J. Oh, A. Y. Zhu, F. Capasso, *Science* **2016**, *352*, 1190.
- [50] J. Lin, P. Genevet, M. A. Kats, N. Antoniou, F. Capasso, *Nano Lett.* **2013**, *13*, 4269.
- [51] J. Zeng, J. Gao, T. S. Luk, N. M. Litchinitser, X. Yang, *Nano Lett.* **2015**, *15*, 5363.
- [52] A. Artar, A. A. Yanik, H. Altug, *Nano Lett.* **2011**, *11*, 1685.
- [53] A. Silva, F. Monticone, G. Castaldi, V. Galdi, A. Alù, N. Engheta, *Science* **2014**, *343*, 160.
- [54] Z. Li, M. Mutlu, E. Ozbay, *J. Opt.* **2013**, *15*, 023001.
- [55] Z. Wang, F. Cheng, T. Winsor, Y. Liu, *Nanotechnology* **2016**, *27*, 412001.
- [56] Y. Cui, L. Kang, S. Lan, S. Rodrigues, W. Cai, *Nano Lett.* **2014**, *14*, 1021.
- [57] Z. Wang, Y. Wang, G. Adamo, B. H. Teh, Q. Y. S. Wu, J. Teng, H. Sun, *Adv. Opt. Mater.* **2016**, *4*, 883.
- [58] A. B. Khanikaev, N. Arju, Z. Fan, D. Purtseladze, F. Lu, J. Lee, P. Sarriugarte, M. Schnell, R. Hillenbrand, M. A. Belkin, G. Shvets, *Nat. Commun.* **2016**, *7*, 12045.
- [59] L. D. Barron, *Molecular Light Scattering Optical Activity*, Cambridge University Press, Cambridge, UK **2004**.
- [60] W. W. Parson, *Modern Optical Spectroscopy*, Springer, Berlin, Heidelberg **2007**.
- [61] Y. Zhao, A. Alù, *Phys. Rev. B* **2011**, *84*, 205428.
- [62] M. Kuttge, F. J. G. de Abajo, A. Polman, *Opt. Express* **2009**, *17*, 10385.
- [63] E. Prodan, C. Radloff, N. J. Halas, P. Nordlander, *Science* **2003**, *302*, 419.
- [64] C.-p. Huang, Y. Zhang, Q.-j. Wang, X.-G. Yin, G.-d. Wang, J.-q. Liu, Y.-y. Zhu, *J. Phys. Chem. C* **2011**, *115*, 24621.
- [65] Y. Chen, J. R. Chu, X. F. Xu, *ACS Photonics* **2016**, *3*, 1689.
- [66] C. Menzel, C. Rockstuhl, F. Lederer, *Phys. Rev. A* **2010**, *82*, 053811.
- [67] S. P. Rodrigues, S. Lan, L. Kang, Y. Cui, W. Cai, *Adv. Mater.* **2014**, *26*, 6157.